

Molybdenum-Doped Nickel Disulfide (NiS₂:Mo) Microspheres as an Active Anode Material for High-Performance Durable Lithium-Ion Batteries

Paskalis Sahaya Murphin Kumar, Vinothkumar Ponnusamy, Hyoung-il Kim, Martín Adelaido Hernández-Landaverde, Siva Kumar Krishnan,* and Umapada Pal



Cite This: *ACS Appl. Energy Mater.* 2022, 5, 6734–6745



Read Online

ACCESS |



Metrics & More



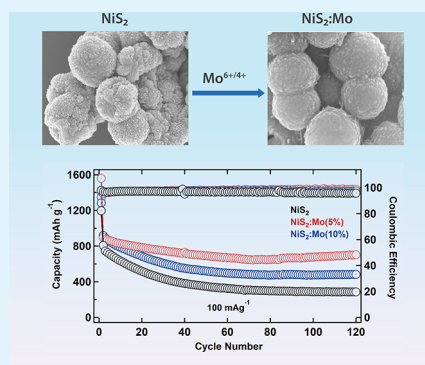
Article Recommendations



Supporting Information

ABSTRACT: Transition-metal sulfides (TMSs) are promising anode materials for lithium-ion batteries (LIBs) as they exhibit anomalously high specific capacities. However, the electrodes made on TMSs possess low electronic conductivity and poor specific capacity retention, which hinder their application in LIBs. Herein, we report a one-step, simple, hydrothermal technique for synthesizing molybdenum-doped nickel disulfide (NiS₂:Mo) microspheres with varying Mo contents (0, 5, and 10 wt %) and their performance as anode materials in LIBs. Mo doping was found to improve the electronic conductivity, structural stability, and reduce charge transfer resistance between the electrode/electrolyte interface of NiS₂ microspheres, thereby achieving a superior electrochemical performance in LIBs. The anode made of NiS₂:Mo microspheres with 5 wt % Mo registered a maximum specific capacity and cycling durability. It delivered an outstanding initial specific capacity of 1605 mAh g⁻¹ at 0.1 Ag⁻¹ and exhibited exceptional cycling stability with a reversible discharge capacity retention of 713.3 mAh g⁻¹ after 120 cycles and Coulombic efficiency of 98.42%. Such exceptionally high specific capacity and high charge–discharge capacity retention of the NiS₂:Mo (5%) microspheres indicate that the material is a promising anode material for LIBs and other advanced energy storage applications.

KEYWORDS: nickel disulfide, molybdenum doping, green fabrication, Piper-longum fruit extract, anode materials, lithium-ion battery



1. INTRODUCTION

Rechargeable lithium-ion batteries (LIBs) have drawn much attention in recent times as one of the most attractive class of energy storage devices, capable of meeting future energy demands in a sustainable way.^{1,2} Since the first rechargeable LIBs were commercially developed by Sony Corporation, Japan, in 1991, using LiCoO₂/C as an active electrode material,³ LIBs become ubiquitous in everyday life because of their versatile applications, including in electronic devices, electric vehicles, energy storage grids, etc.^{4–6} However, the utilization of LIBs on a large scale has been significantly hindered because of the low energy density of anode materials.⁷ Although graphite-based materials have been employed widely for LIB anodes, they often exhibit a relatively low specific capacity. In fact, the theoretical specific capacity of graphite is only 372 mAh g⁻¹. Thus, its practical utilization in LIBs has fallen short of expectation.⁸ To improve the energy storage capacity and cycling durability of LIBs, a tremendous research effort has been devoted recently for developing efficient and stable anode materials.^{9–11} Specifically, anode materials based on transition-metal oxide (TMO) nanostructures^{12,13} and their carbonaceous hybrid composites¹⁴ have attracted much attention, since they can deliver outstanding

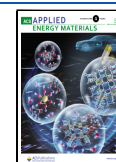
specific capacities in 700–1200 mAh g⁻¹ range, which are about 3-fold higher than the specific capacities of commercial graphitic carbon-based anodes.¹³ However, these electrodes still suffer from the large volume expansion during charge–discharge cycling, affecting the cycling stability of the LIBs.¹⁵ Hence, the development of anode materials that are capable of delivering high charge capacity and high cycling stability is of immense importance for meeting the growing demand of high-capacity anodes for LIBs.

Recently, nanostructured transition-metal sulfides (TMSs) have gained increasing attention due to their remarkable lithium storage performance, exceptionally high specific capacity and prolonged cycling stability both in LIBs and sodium-ion batteries (SIBs).^{16–18} For instance, TMS nanostructures such as ZnS,¹⁹ Cu₂S,²⁰ NiS₂,²¹ CoS₂,²² MoS₂,²³ and FeS₂,²⁴ have been utilized as high-capacity anodes in LIBs/

Received: January 30, 2022

Accepted: May 31, 2022

Published: June 13, 2022



SIBs due to their excellent lithium storage performance and unique electronic structures.²⁵ In particular, nickel disulfide (NiS_2) is seen to be chemically stable among the other nickel sulfide phases like NiS_2 , Ni_3S_2 , Ni_3S_4 , and Ni_7S_6 with a considerably high theoretical specific capacity (807 mAh g^{-1}).²¹ Unfortunately, NiS_2 also exhibits low electronic conductivity and lacks structural stability, thus inevitably undergoes volume expansion and structure failure during longer charge–discharge cycling during the lithium insertion/exertion process, resulting in poor cycling stability and severe pulverization.¹⁸ One successful approach to tackle these issues of anode materials is the doping TMOs/TMSs with metal ions. Several mono- and multivalent dopant ions, such as Cu^{2+} , Co^{2+} , Mo^{6+} , Nb^{5+} , Cr^{3+} , Ti^{4+} , etc., were used to dope TMOs/TMSs and tested as anode materials for LIBs.^{24,26–28} Among the tested dopants, Mo was seen to improve the specific capacity and cycling stability of TMO/TMS electrodes remarkably.^{29,30} For instance, Chen et al.³⁰ showed that doping of porous WO_2 with Mo stabilizes its structure and improves its electronic conductivity, resulting in its performance enhancement as the electrode material in LIBs. Recently, we have shown that Mo doping in Cu_2O -based anodes can substantially enhance its specific capacity (up to 1128 mAh g^{-1} at 0.1 Ag^{-1}) and cycling stability in LIBs.³¹ Considering the impressive performance in previous studies, we considered Mo doping in NiS_2 microspheres to utilize them as the anode material for LIBs. As the average Shannon radii³² of Mo^{6+} (0.59 \AA)³¹ and Ni^{2+} (0.69 \AA) ions are relatively close, the replacement of Ni^{2+} by Mo^{6+} in the NiS_2 lattice is highly feasible. Previous studies have revealed that Mo^{6+} ions can substitute the Ni^{2+} ions from the NiS_2 lattice effectively at relatively low Mo concentrations ($<1 \text{ mol } \%$). Above this concentration, only a fraction of Mo^{6+} ions occupies the Ni^{2+} sites, segregating the remaining fraction toward the surface of NiS_2 .³³ Moreover, Mo doping can reduce the irreversible capacity loss due to lower side reactions of the electrode with electrolytes and promote the fast ionic transport at the surface of anode materials.³⁴

To enhance the electrochemical performance of these anodes further, the TMSs and TMOs with micro-/nanosphere morphologies composed of small nanosized particles or multishell structures have been synthesized and utilized as anode materials for LIBs with good performances.^{19,35,36} These microstructures could provide a large number of surface sites for lithium storage, promote the transport of Li^+ and e^- , and also buffer the volume change during repeated cycling.³⁷ Over the past few years, numerous synthetic approaches such as wet-chemical synthesis,³⁸ template-assisted synthesis,³⁹ and hydrothermal and solvothermal processes have been explored for fabricating TMS/TMO microspheres.¹⁹ Among the explored methods, green-solvent-assisted hydro-/solvothermal processes have been recognized as attractive and efficient synthesis platforms for fabricating uniform-sized TMS/TMO microstructures.⁴⁰ Recently, green and environmentally friendly solvents such as deep eutectic solvents (DESs)⁴¹ and various plant/fruit extracts³¹ have been utilized for the hydro-/solvothermal synthesis of TMO and TMS microstructures in a controlled manner. Specifically, the *Piper-longum* extract obtained from long *Piper-longum* fruits has been utilized as a solvent and a stabilizing agent in the synthesis of metallic NPs^{42,43} and metal oxide nanostructures.^{31,42} The extract obtained from the long *Piper-longum* fruits has been traditionally known as a medicine for treating a variety of diseases including cancer.⁴² Previous studies have revealed that *Piper-*

longum fruit extract contains piperine, piperlongumine, sylvatin, pipermonaline, and several phytochemicals containing phenol and/or polyol groups.⁴³ The presence of such groups in the extract plays a key role and makes the extract an effective stabilizing and reducing agent for various metal ions.^{43,44}

In this article, we present a one-step hydrothermal process for the synthesis of porous NiS_2 and Mo-doped NiS_2 microspheres using the *Piper-longum* fruit extract as a solvent. NiS_2 :Mo microspheres with different Mo contents were prepared and utilized as anode materials for LIBs. The anode fabricated with NiS_2 :Mo (5%) microspheres manifested the best electrochemical performance with a specific capacity as high as 1605 mAh g^{-1} at 0.1 A g^{-1} , high rate capability, and excellent cycling stability. The superior performance of the porous NiS_2 :Mo (5%) microspheres has been associated with their improved structural stability, electrical conductivity, and a fast ion diffusion between the anode and the electrolyte solution.

2. EXPERIMENTAL SECTION

2.1. Materials. Nickel(II) nitrate hexahydrate ($\text{Ni}(\text{NO}_3)_2 \cdot 6\text{H}_2\text{O}$, 99.999%), thiourea (NH_2CSNH_2 , 99.0%), ammonium molybdate tetrahydrate, ($(\text{NH}_4)_6\text{Mo}_7\text{O}_{24} \cdot 4\text{H}_2\text{O}$), and ethyl alcohol (anhydrous, $\geq 99.5\%$) were purchased from Sigma-Aldrich, Korea. All of the chemicals were of analytic grade and utilized as received without further purification. Deionized water ($\rho > 18.2 \text{ } \Omega\text{-cm}$) was used for all synthesis and electrochemical experiments.

2.2. Preparation of *Piper-longum* Fruit Extract. Ripped *Piper-longum* fruits were collected from *Piper-longum* (long pepper) plants grown in the southern part of India. The collected *Piper-longum* fruits were first washed with DI water several times to remove surface attached contaminations such as dust and then allowed to dry under shade to eliminate the moisture. After drying, the fruits were ground well in a commercial electric mixture grinder, obtaining a fine powder, which was utilized to prepare the *Piper-longum* fruit extract. About 0.5 g of the prepared powder was dispersed in 50 mL of ethanol under magnetic stirring for 30 min. Finally, the solution mixture was filtered using a Whatman filter paper to have a homogeneous *Piper-longum* fruit extract, which was stored at ambient temperature and utilized for the synthesis of NiS_2 and NiS_2 :Mo microspheres.

2.3. Synthesis of NiS_2 and NiS_2 :Mo microspheres. NiS_2 and NiS_2 :Mo microspheres were prepared by a single-step, *Piper-longum* extract-assisted hydrothermal process, where the fruit extract was used as an effective solvent. In a typical synthesis process of the NiS_2 microsphere, 5 mL (50 mmol) of nickel nitrate hexahydrate ($\text{Ni}(\text{NO}_3)_2 \cdot 6\text{H}_2\text{O}$) and 5 mL (50 mM in DI water) of thiourea (NH_2CSNH_2) were mixed with 50 mL of *Piper-longum* fruit extract under magnetic stirring at room temperature. After 1 h of magnetic stirring, the reaction mixture was transferred to a 100 mL Teflon-lined stainless-steel autoclave. The capped autoclave containing the reaction mixture was then heated to $200 \text{ }^\circ\text{C}$ (at $5 \text{ }^\circ\text{C}/\text{min}$ heating rate) and kept at this temperature for 12 h. After that, the autoclave was cooled to ambient temperature. The obtained product was separated by centrifugation, washed four times with water and ethanol, and dried at $60 \text{ }^\circ\text{C}$ for 6 hours. The Mo-doped NiS_2 (NiS_2 :Mo) samples with varied Mo contents (0.0, 5.0, and 10.0 wt %) were prepared using a similar protocol, and only the reaction mixture of $\text{Ni}(\text{NO}_3)_2 \cdot 6\text{H}_2\text{O}$ and NH_2CSNH_2 was allowed to magnetic stirring for 2 h in the *Piper-longum* extract solvent. Then, different amounts of a molybdenum precursor ($(\text{NH}_4)_6\text{Mo}_7\text{O}_{24} \cdot 4\text{H}_2\text{O}$) were added to the reaction mixture before its hydrothermal treatment.

2.4. Characterization of Doped and Undoped Microspheres. **2.4.1. Morphology and Structural Characterization.** Crystallinity and the crystal structure of the as-grown microsphere samples were examined by X-ray diffraction (XRD, X'Pert PRO PANalytical) utilizing a $\text{Cu K}\alpha$ X-ray radiation source ($\lambda = 0.15406 \text{ nm}$). A field emission-scanning electron microscope (FE-SEM, Hitachi SU800) coupled with an energy-dispersive X-ray spectrom-

Scheme 1. Schematic Presentation of the Steps Involved in the *Piper-longum* Fruit Extract-Assisted Hydrothermal Process Utilized for the Synthesis of NiS₂:Mo Microspheres

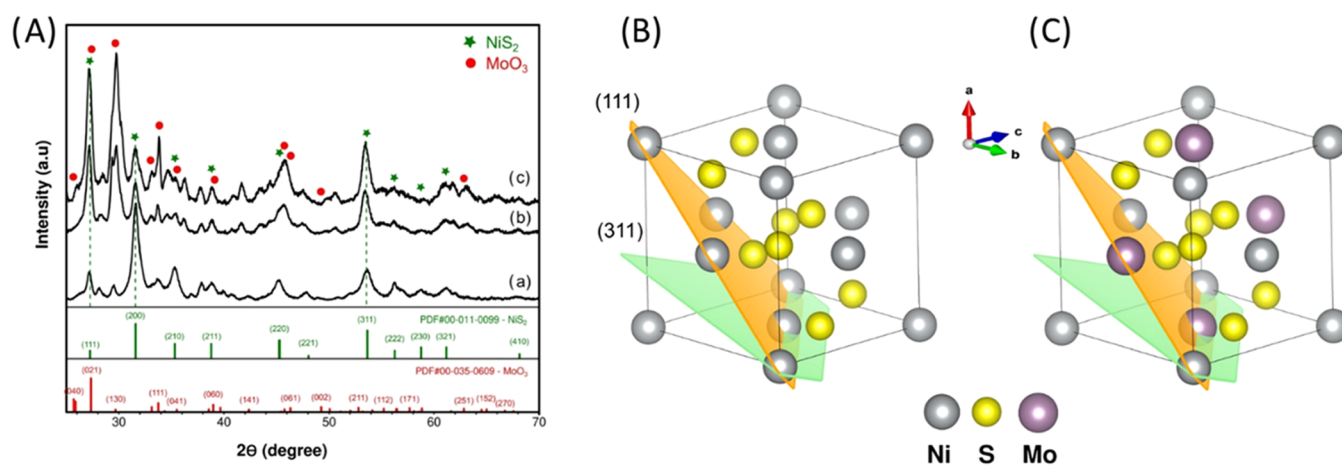
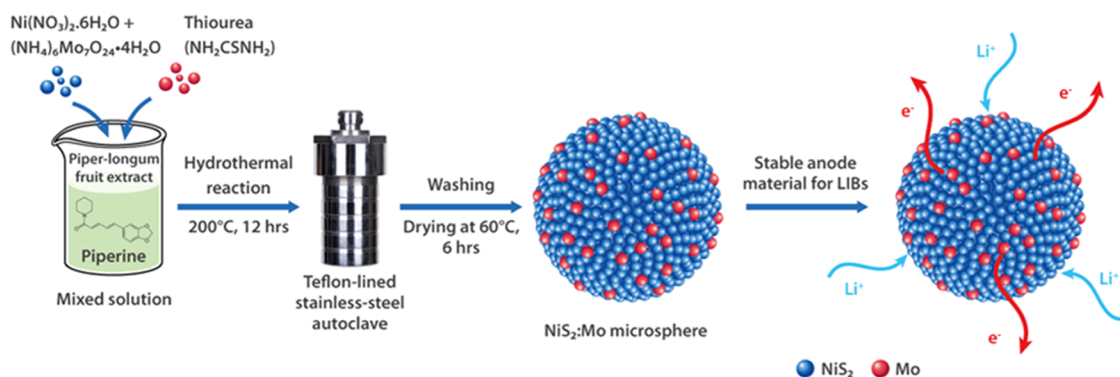


Figure 1. (A) Typical XRD patterns of (a) NiS₂, (b) NiS₂:Mo (5%), and (c) NiS₂:Mo (10%) microspheres. The red and green vertical lines correspond to the peak positions of standard NiS₂ and MoO₃, respectively. (B) Structure of pure NiS₂ and (C) possible Mo dopant sites in NiS₂ lattice.

eter (EDX) operated at 15 kV was utilized to analyze the morphology, surface structure, and composition of the synthesized microspheres. A JEOL JE2300T transmission electron microscope (TEM) operating at 120 kV was utilized to record the TEM and HR-TEM images for a detailed analysis of the surface morphology and fine structure of the samples. X-ray photoelectron spectroscopy (XPS) was utilized to analyze the composition of the samples and the oxidation states of their constituting elements. An Omicron (Nanotechnology, Germany) spectrometer operating at ultrahigh vacuum (1×10^{-10} Torr) and a Al K α radiation source (1486.6 eV) was utilized for this purpose.

2.4.2. Electrochemical Characterization. For the fabrication of LIB anodes, first, a homogeneous paste was prepared by mixing the active material (as-synthesized sample), 10 wt % polyacrylic acid-carboxymethyl cellulose binder, and 15 wt % acetylene black (AB) in DI water. The viscous slurry was then cast over a clean commercial copper foil (Sigma-Aldrich, 99.0%) by doctor blading and allowed to dry in a vacuum oven at 120 °C for 12 h. The deposited film was then pressed to accomplish an intimate contact between the active material and the copper current collector. The area of the anode was about 1.539 cm², and the estimated average loading (active material) was about 1.5 mg cm⁻². Lithium metal foils were used both as the reference and the counter electrode, while a thin polypropylene membrane was employed as a separator. For half-cell fabrication, a mixture of 1M LiPF₆ in ethylene carbonate (EC) and dimethyl carbonate (DMC) in a 1:1 volume ratio was employed as an electrolyte. All of the electrochemical measurements were carried out by assembling 2032 standard battery coin cells inside an argon-filled glovebox. An electrochemical impedance spectrometer (EIS, Zive MP2, Seoul, South Korea) in a multichannel electrochemical workstation was employed to record the EIS spectra and CV profiles.

3. RESULTS AND DISCUSSION

As shown in Scheme 1, pure NiS₂ and Mo-doped NiS₂ microspheres of uniform sizes were synthesized through a single-step hydrothermal process in the presence of thiourea and the *Piper-longum* fruit extract. Previous studies revealed that the S atoms of the thiourea molecules have a strong binding affinity with different metal cations, such as Zn²⁺, Ni²⁺, etc.^{19,45} In the present case, during the hydrothermal reaction, Ni²⁺ ions from the Ni(NO₃)₂·6H₂O precursor react with S²⁻ ions generated from the decomposition of thiourea (NH₂CSNH₂). As a result, the Ni²⁺ ions are reduced and form NiS₂ nanoparticles. In the case of Mo-doped NiS₂, the S²⁻ ions from thiourea react with the Ni²⁺ and Mo^{4+/6+} ions during the hydrothermal treatment to form Mo-doped NiS₂ NPs. The long-chain piperine present in the *Piper-longum* fruit extract contains phenolic groups, which serve as a surfactant for the controlled growth of NiS₂ or NiS₂:Mo nanoparticles.³¹ The slow reduction of metal ions by thiourea under the hydrothermal reaction conditions in the presence of *Piper-longum* extract leads to a controlled aggregation of small particles, producing porous spherical microstructures. For a better understanding of the role of *Piper-longum* fruit extract in the formation of microsphere structures, controlled synthesis of bare NiS₂ and NiS₂:Mo (5%) samples was carried out by replacing the *Piper-longum* fruit extract with ethanol as a solvent keeping all other synthesis conditions the same. Figure

S1 (Supporting Information) shows the SEM images of the bare NiS₂ and NiS₂:Mo (5%) samples obtained without *Piper-longum* fruit extract in the reaction mixture. As can be seen, the final products were not well-defined microsphere structures, instead, microstructures of flower-like morphology were formed. This clearly indicates that the *Piper-longum* fruit extract plays a key role in the formation of microsphere morphologies.

Powder X-ray diffraction (XRD) analysis was performed to analyze the crystalline structure and phase of the as-prepared microsphere samples. Figure 1A shows the XRD patterns of the pure NiS₂, NiS₂:Mo (5%), and NiS₂:Mo (10%) samples. As can be noticed in Figure 1A, the pure NiS₂ samples revealed several well-defined diffraction peaks, and the position of all of the peaks match well with the standard peak positions of cubic NiS₂ in pyrite phase (JCPDS No. 00-011-0099).²¹ Appearance of intense and well-defined diffraction peaks indicates the good crystallinity of the as-prepared NiS₂ sample. XRD spectra of the NiS₂:Mo samples revealed additional peaks, which could be readily indexed to the MoO₃ phase (JCPDS No. 00-005-0600).⁴⁶ It is important to mention that no obvious peaks corresponding to the other phase such as MoS₂ were found. Notably, the intensity of the diffraction peaks associated with the (111) and (311) planes of NiS₂ increased with the increase of Mo content, indicating the incorporation of Mo^{4+/6+} ions through Ni²⁺ substitution in the NiS₂ lattice. Considering that the ionic radii of Mo⁴⁺ (0.65 Å) and Mo⁶⁺ (0.59 Å) ions are relatively close to the ionic radius of Ni²⁺ (0.69 Å) ions, it is reasonable to consider that Mo^{4+/6+} ions occupy Ni²⁺ sites in the NiS₂ lattice. However, doping a higher Mo concentration could increase the amount of Ni²⁺ ions at the expense of Ni³⁺ ions.³³ Average crystallite sizes estimated from the full width at half-maximum values of the XRD peaks were about 18.0, 21.6, and 17.1 nm for the pure NiS₂, NiS₂:Mo (5%), and NiS₂:Mo (10%) samples, respectively. Based on the XRD results, the Mo site occupancy in the unit cell of NiS₂ is proposed. NiS₂ bears a cubic crystal structure with the space group *Pa*3 (205), in which the Ni atoms occupy the sites in the fcc sublattice (Figure 1B).⁴⁷ The doped Mo atoms incorporate into the NiS₂ lattice, possibly by replacing the Ni²⁺ ions in the {111} and {311} lattice planes as displayed in Figure 1C.

The morphological characteristics of the as-obtained pure NiS₂ and Mo-doped NiS₂ microspheres were explored using field emission-scanning electron microscopy (FE-SEM). Figure 2 shows the low- and high-magnification SEM images of NiS₂, NiS₂:Mo (5%), and NiS₂:Mo (10%) samples. The formation of uniform microspheres of about 500 nm diameter in the pure NiS₂ sample can be clearly seen in the low-magnification SEM image presented in Figure 2a. A high-magnification SEM image (Figure 2b) of the sample revealed that the NiS₂ microspheres are composed of tiny particles assembled together, which act as the building blocks of the microspheres. Due to the same reason, the microspheres have rough surfaces.

In the case of the NiS₂:Mo (5%) sample (Figure 2c,d), although the original spherical morphology was preserved, the surface roughness of the microspheres increased, which was due to the partial substitution of Ni²⁺ by Mo⁶⁺ atoms and the segregation of the remaining Mo atoms toward the surface of NiS₂. With the increase of Mo concentration from 5 to 10 wt %, the roughness of the NiS₂ microsphere surface increased (Figure 2e,f). This could be mainly because of the high Mo content in the reaction mixture, as a major fraction of the Mo atoms segregates to the NiS₂ surface. Moreover, with higher

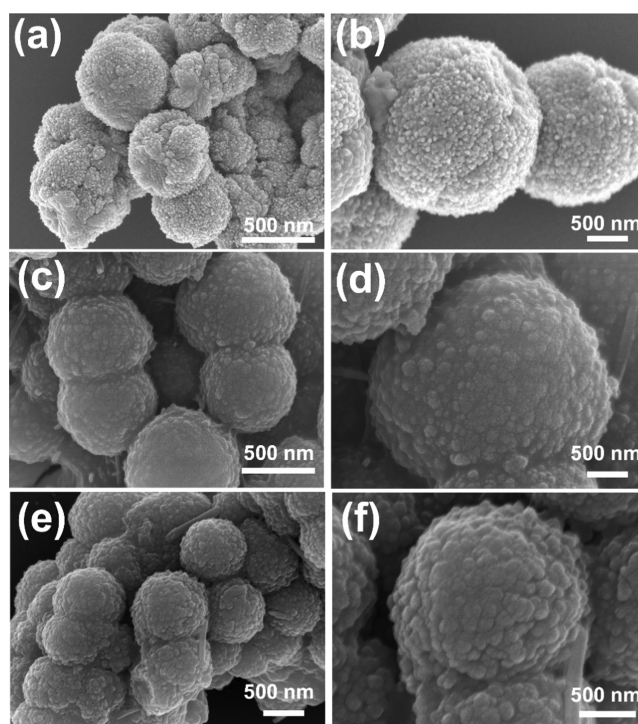


Figure 2. Typical SEM images of (a, b) pure NiS₂, (c, d) NiS₂:Mo (5%), and (e, f) NiS₂:Mo (10%) microsphere samples. The images in the left and right columns correspond to low- and high-magnification images, respectively.

Mo doping (about 10%), the particle size is found to be decreased (Figure 2e,f), which is consistent with the crystallite size estimated from XRD peaks. Such a decrease of particle size is due to the partial incorporation of Mo ions at the Ni²⁺ sites and subsequent surface segregation of remaining Mo atoms, as has been observed by other research groups.^{30,33}

To further explore the surface structure and morphology of the as-prepared NiS₂:Mo samples, they were analyzed in a transmission electron microscope (TEM). Figure 3a,b shows the typical TEM images of the NiS₂:Mo (5%) microsphere sample. The spherical shape and rough surface morphology of the microstructures are very clear in the TEM images. The TEM-estimated particle size of the microstructures is ~500 nm, which is in good agreement with the size estimated from their SEM analysis. Figure 3c shows the typical high-resolution TEM (HR-TEM) image of a NiS₂:Mo (5%) microsphere sample. The crystalline MoO₃ and NiS₂ regions in the microsphere can be clearly distinguished from the respective interplanar spacing in the magnified sections (marked by square boxes in Figure 3c) presented in Figure 3d,e, respectively. As can be seen, the estimated lattice spacing values are about 0.39 and 0.283 nm (Figure 3d,e), which are associated with the (110) plane of MoO₃⁴⁸ and (200) plane of NiS₂,²¹ respectively. Ni, S, and Mo distributions in the microsphere were recorded by EDX mapping. As can be noticed in the EDX mapping images presented in Figure 3f, all three elements remained uniformly distributed in the microspheres. EDX spectra of the samples (Figure S2, Supporting Information) revealed the emissions of Ni, S for NiS₂, and Ni, S, Mo, and O elements for NiS₂:Mo microspheres. The estimated Mo content in the NiS₂:Mo (5%) and NiS₂:Mo (10%) samples was about 4.23 and 8.96 wt % (Table S1, Supporting Information), which are very close to the nominal

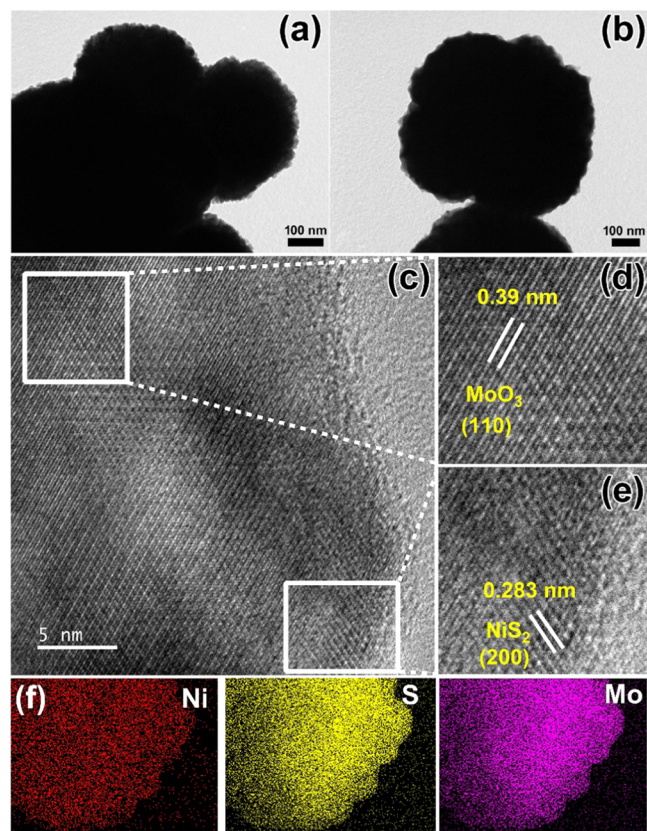


Figure 3. (a, b) Typical TEM images and (c–e) HR-TEM images of the NiS₂:Mo (5%) microspheres. (f) EDX elemental mapping images showing the uniform distribution of Ni, S, and Mo elements in the microspheres.

Mo contents in the corresponding reaction mixtures used for the hydrothermal reaction.

To identify the elemental composition and valence states of the constituting elements, the NiS₂ and NiS₂:Mo microsphere samples were analyzed by X-ray photoelectron spectroscopy (Figure 4). The survey XPS spectra of the samples presented in Figure 4a clearly show the appearance of emission peaks of Ni, S, Mo, and O elements in the NiS₂:Mo microsphere samples and the absence of Mo emission for the pure or undoped NiS₂ microsphere sample, confirming their purity. The core-level Ni 2P emission of the NiS₂:Mo (5%) sample (Figure 4b) revealed peaks at binding energies 871.1 and 853.9 eV, associated with the 2P_{1/2} and Ni 2p_{3/2} spin–orbit splitting of Ni³⁺ species.^{49–51} The two satellite peaks that appeared around 276.9 and 258.6 eV are associated with the Ni²⁺ state of nickel.^{51,52} The results confirm that Ni in the NiS₂:Mo (5%) sample remained in Ni³⁺ and Ni²⁺ oxidation states. Figure 4c shows the S 2P core-level emission of the NiS₂:Mo (5%) sample. The spectrum revealed two intense peaks centered at around 169.1 and 164.7 eV binding energies, which correspond to the 2P_{1/2} and 2P_{3/2} orbitals of divalent sulfide ions S^{2–} in NiS₂.^{26,52} Finally, the core-level Mo 3d emission of the sample (Figure 4d) reveals that the bands corresponding to Mo 3d_{5/2} and Mo 3d_{3/2} orbitals of Mo⁶⁺ peaked around 232.4 and 235.5 eV, respectively.^{46,53} Also, two low-intensity peaks appeared around 230.2 and 234.6 eV, which correspond to the Mo 3d_{5/2} and Mo 3d_{3/2} orbitals of Mo⁴⁺.⁵⁴ Although these results indicate that Mo remains in Mo⁶⁺/Mo⁴⁺ mixed oxidation states in the NiS₂:Mo (5%) sample from the areas of the

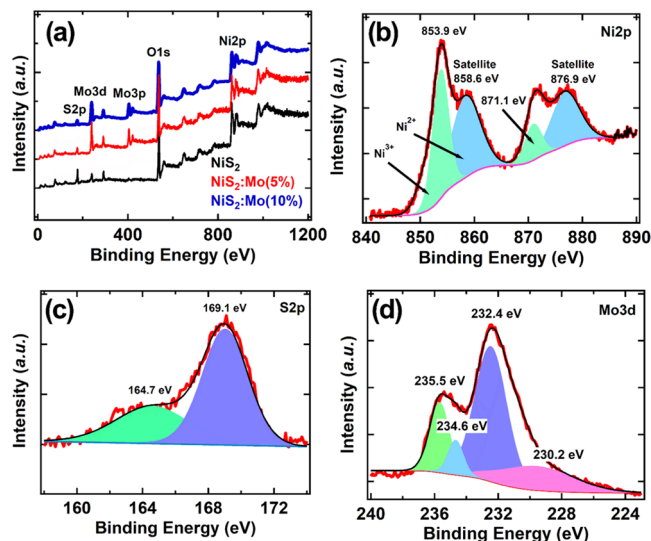
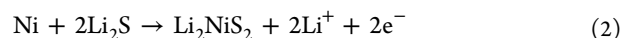
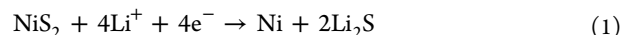


Figure 4. XPS (a) survey scans of the pure and Mo-doped NiS₂ microspheres. (b) Ni 2P, (c) S 2P, and (d) Mo 3d core-level spectra of the NiS₂:Mo (5%) microsphere sample, along with their deconvoluted components.

deconvoluted bands in Figure 4d, we can see that only a small fraction of Mo atoms in the sample remains in Mo⁴⁺ oxidation state.

The lithium storing properties of the electrodes made of as-prepared NiS₂:Mo (5%) microspheres were first studied by cyclic voltammetry (CV). Figure 5a presents the typical CV curves of the electrode fabricated with NiS₂:Mo microspheres with 5 wt % Mo incorporation in the first three successive sweeping cycles over a potential range of 0.01 to 3.0 V (*vs* Li⁺/Li) at 0.1 mV s^{–1} scan rate. In the first cathodic scan, two peaks appeared at around 1.86 and 0.742 V (*vs* Li⁺/Li). While the peak appeared at 1.86 V is associated with Li⁺ insertion and conversion of NiS₂ into metallic Ni,⁵⁰ the peak appeared at 0.742 V can be ascribed to the irreversible decomposition of the electrolyte solution, followed by an irreversible formation of a solid electrolyte interface (SEI) film over the surface of the electrode material.^{55,56} Notably, after the first cycle, the height of the peak at 0.742 V significantly reduced, suggesting that the SEI film has been formed during the first cycle. In the following first anodic scan, an intense peak appeared at 0.992 V and two less intense peaks appeared around 1.35 and 2.05 V (*vs* Li⁺/Li). The peak appeared at 0.992 V is related to the partial dissolution of the SEI film.²⁷ On the other hand, the peak appeared around 2.05 V is associated with the delithiation of Li⁺ and oxidation of metallic Ni and formation of NiS₂,⁵⁷ and the peak appeared around 1.35 V corresponds to the oxidation of Mo to form MoO₃.⁵⁸ These conversion reactions can be described by the following equations⁵⁹



It should be noted that the oxidation peak at 1.358 V disappeared in the 3rd cycle, while the other peaks remained unchanged, which indicates that the incorporation of Mo in NiS₂ reduces the conversion reaction reversibility slightly, as observed in previous studies.⁵⁸ After the first CV cycle, the observed reduction peaks during the first cycle appeared around 1.86 and 0.742 V were shifted to 1.87 and 0.73 V, and

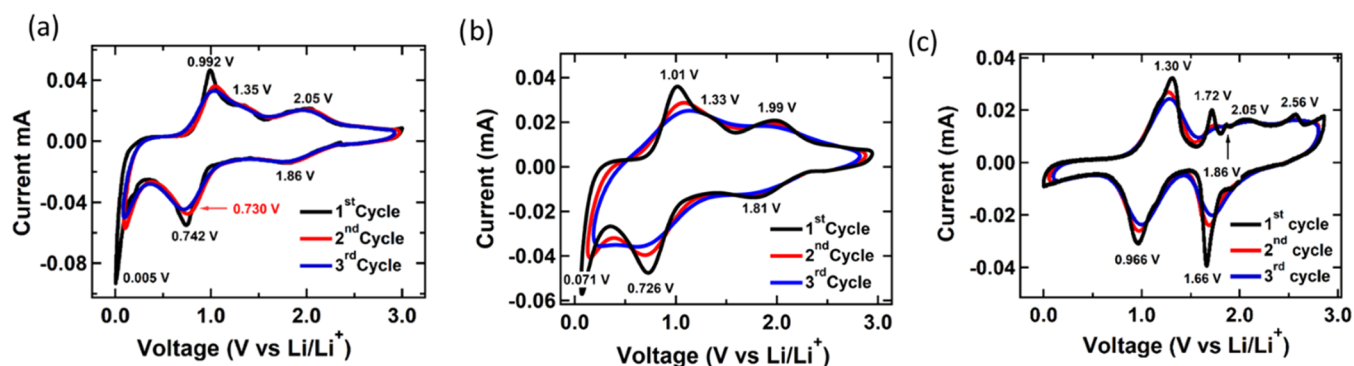


Figure 5. CV curves of (a) NiS₂:Mo (5%), (b) NiS₂:Mo (10%), and (c) bare NiS₂ microsphere electrodes in the 1st, 2nd, and 3rd sweeping cycles recorded in the 0.01–3.0 V (*vs* Li/Li⁺) range at a scan rate of 0.1 mV s⁻¹.

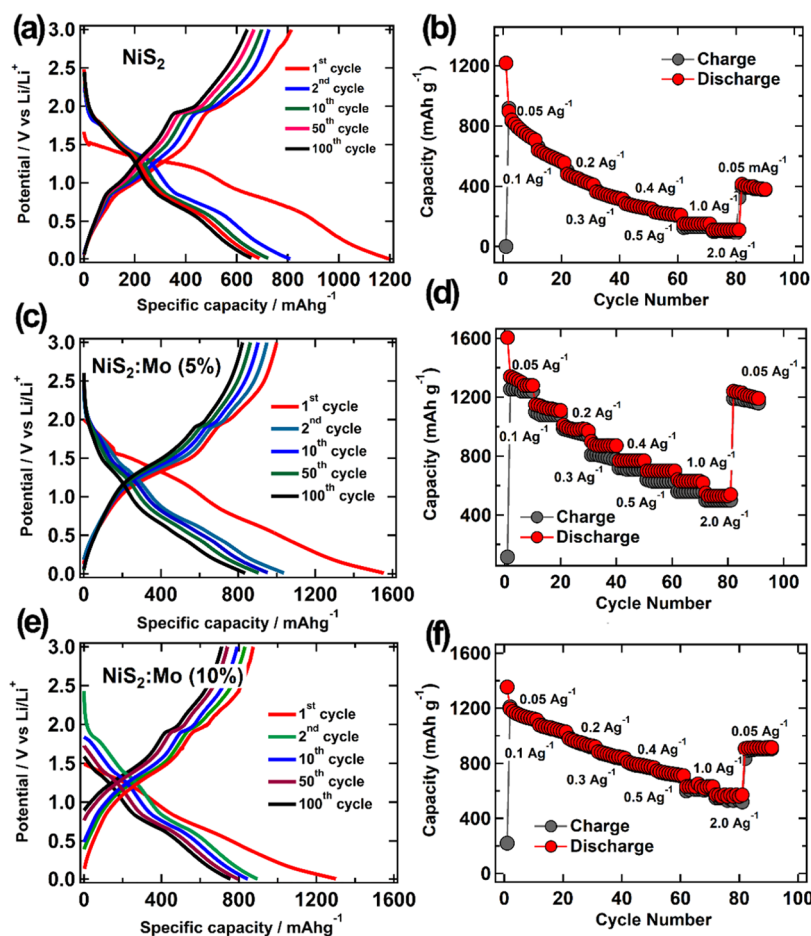


Figure 6. Typical galvanostatic charge–discharge curves of (a) pure NiS₂, (c) NiS₂:Mo (5%), and (e) NiS₂:Mo (10%) microspheres in the potential window 0.01–3.0 V (*vs* Li/Li⁺) at a current density of 0.1 Ag⁻¹. (b, d, f) Rate capability of pure NiS₂, NiS₂:Mo (5%), and NiS₂:Mo (10%) microspheres at various current densities between 0.05 and 2.0 A g⁻¹.

the oxidation peaks at 0.992 and 2.05 V were shifted to 1.01 and 2.04 V, respectively. The shifts in the redox peaks during the later cycles could be ascribed to the improved diffusion kinetics of Li ions.²⁷ Notably, the redox peaks exhibit identical shape and position during the second and third cycles, which implies the excellent cycling stability of the NiS₂:Mo electrode.⁶⁰

For a better comparison, the CV profiles of NiS₂:Mo (10%) and bare NiS₂ microsphere electrodes were recorded at a scan rate of 0.1 mVs⁻¹ (Figure 5b,c). The CV curve in the first cycle of the NiS₂:Mo (10%) electrode exhibited redox peaks similar

to that of the NiS₂:Mo (5%) electrode, with a slight variation in shape. The CV curve for the bare NiS₂ electrode acquired in the first cycle revealed two prominent cathodic peaks located at 1.66 and 0.966 V, which are associated with the conversion of NiS₂ to metallic Ni and the formation of SEI films on the electrode surface, respectively. On the other hand, the first anodic scan of the bare NiS₂ electrode revealed oxidation peaks located at 1.30 V is attributed to the decomposition of SEI films, whereas the peaks that appeared at 1.72 and 2.05 V correspond to the formation of Li_xNiS₂ and conversion of Ni

into NiS₂, respectively.^{21,62} Notably, the intensities of the redox peaks for both the NiS₂:Mo (10%) and bare NiS₂ electrodes become weaker in the following cycles, indicating the low stability of the NiS₂:Mo (10%) and pure NiS₂ microsphere electrodes.

The electrochemical activity of the NiS₂:Mo anode toward Li⁺ ion storage performance was studied in 20320-type standard battery coin cells with lithium metal as counter electrodes. To investigate the intrinsic properties of the fabricated electrodes, electrochemical galvanostatic charge–discharge cycling was employed in the potential range 0.01–3.0 V (*vs* Li/Li⁺) at a current density of 0.1 A g⁻¹. Figure 6a,c,e shows the representative galvanostatic charge–discharge curves of the pure NiS₂, NiS₂:Mo (5%), and NiS₂:Mo (10%) electrodes during the 1st, 2nd, 10th, 50th, and 100th cycles. As can be seen, all of the electrodes exhibit a series of plateaus at 1.5 V and below 1 V during the first discharge cycle due to the change of conversion reactions, which is in good agreement with the CV curves presented in Figure 5. The galvanostatic charge–discharge curves presented in Figure 6c indicate that the galvanostatic discharge capacity of the NiS₂:Mo (5%) electrode in its first cycle is about 1554.3 mA g⁻¹, which decreased to 1037.9, 952.83, 906.15, and 836.89 mA g⁻¹ in the subsequent 2nd, 10th, 50th, and 100th cycles, respectively. However, the electrode fabricated with pure NiS₂ microspheres registered discharge capacities of 1197.3, 809.3, 723.1, 688.9, and 657.3 mA g⁻¹, and the electrode fabricated with NiS₂:Mo (10%) microspheres displayed specific discharge capacities of 1296.6, 896, 845.3, 802.4, and 760.0 mA g⁻¹ for the 1st, 2nd, 10th, 50th, and 100th cycles, respectively. The results clearly indicate the superior discharge capacity of the NiS₂:Mo (5%) microspheres in comparison with the pure NiS₂ and NiS₂:Mo (10%) microspheres. Moreover, the change in the discharge capacity for the NiS₂:Mo (5%) sample after the first cycle is very small, indicating that the conversion reaction in the electrode is irreversible. The observed low-capacity loss for the NiS₂:Mo (5%) sample after the 1st cycle can be understood by the fact that decomposition of electrolytes and subsequent formation of a thin SEI film occurred during the 1st cycle, as commonly occurs for the TMS-based anodes operating through conversion reactions.^{61,62} From the galvanostatic charge–discharge curves presented in Figure 6e, we can see that the discharge capacity of the electrode made of NiS₂:Mo (10%) microspheres is considerably lower than the discharge capacity of the electrode prepared with NiS₂:Mo (5%), although it is higher than the discharge capacity if the pure NiS₂ microsphere electrode.

The rate capability performance is regarded to be a critical parameter for the anode materials in LIBs for their successful implementation in commercial applications. Hence, the rate performance of the anodes was further studied at different cycling rates from 0.05 to 2.0 A g⁻¹ and then reverting back to 0.05 A g⁻¹ (Figure 6b,d,f). As shown in Figure 6d, the NiS₂:Mo (5%) electrode exhibits remarkably high rate performance relative to the electrodes made of pure NiS₂ and NiS₂:Mo (10%) microspheres. Specifically, the NiS₂:Mo (5%) microspheres deliver an average discharge capacity of 1310.2, 1110.6, 970.9, 871.4, 770.5, 700.1, 620.1, and 540.4 mA h g⁻¹ on stepwise increase of current density from 0.05 A g⁻¹ to 0.1, 0.2, 0.3, 0.4, 0.5, 1.0, and 2.0 A g⁻¹, respectively. Operating even at a high current density of 2.0 A g⁻¹, the NiS₂:Mo (5%) electrode delivered a high discharge capacity of 540 mA h g⁻¹, maintaining a high specific capacity. Notably, the observed

specific capacity value at a high current density (2.0 A g⁻¹) was about 41.2% of its initial discharge capacity value obtained at a low current density of 0.05 A g⁻¹ and also 1.5-fold greater relative to the theoretical specific capacity of an anode made of graphite (372 mA h g⁻¹).⁸ Importantly, after operating at different current densities, the NiS₂:Mo (5%) microsphere electrode retained a specific capacity as high as 1191.3 mA h g⁻¹ when the applied current density was reversed back to 0.05 A g⁻¹ (Figure 6d), indicating its high rate capability. In contrast, the NiS₂ microsphere electrode (anode) showed poor rate capability, and its specific discharge capacity significantly dropped to 110.5 mA h g⁻¹ at 2.0 A g⁻¹ (Figure 6b). The NiS₂ microsphere electrode registered discharge capacities of 897.6, 555.7, 409.2, 313.6, 252.6, 207.5, 150.6, and 110.5 mA h g⁻¹ at current densities of 0.05, 0.1, 0.2, 0.3, 0.4, 0.5, 1.0, and 2.0 A g⁻¹, respectively. Upon reversing back, the current density to 0.05 A g⁻¹, it could recover only 380.8 mA h g⁻¹, which is significantly lower than the recovered current density by the NiS₂:Mo (5%) microsphere electrode (1191.3 mA h g⁻¹). Interestingly, at higher Mo contents, i.e., the NiS₂ microspheres with 10 wt % Mo doping (NiS₂:Mo (10%)) revealed a lower rate capability in comparison with the NiS₂:Mo (5%) microspheres. As shown in Figure 6f, the NiS₂:Mo (10%) electrode recorded discharge capacities of 1122.4, 1028.3, 919.7, 837.3, 772.3, 711.5, 630.6, and 570.2 mA h g⁻¹ at 0.05, 0.1, 0.2, 0.3, 0.4, 0.5, 1.0, and 2.0 A g⁻¹ current densities, respectively. When reverted back the current density value to 0.05 A g⁻¹, the electrode recovered a specific capacity of 914.4 mA h g⁻¹, which is significantly lower than the recovered specific capacity of the NiS₂:Mo (5%) electrode (1191.3 mA h g⁻¹). The low-rate performance of the NiS₂:Mo (10%) electrode is probably attributed to the lower structural stability of the NiS₂ microspheres upon high Mo loading (i.e., above 5%).

The cycling stability of the fabricated anodes was also studied at a higher current density of 100 mA g⁻¹. Figure 7

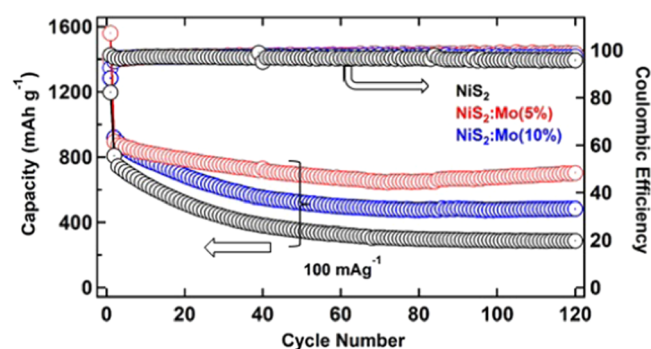


Figure 7. Comparison of long-term cycling stability and corresponding CEs of pure NiS₂, NiS₂:Mo (5%), and NiS₂:Mo (10%) at a charge density of 100 mA g⁻¹ for 120 cycles.

shows the comparison of cycling stability performance and Coulombic efficiencies (CEs) of the pure NiS₂, NiS₂:Mo (5%), and NiS₂:Mo (10%) microspheres. As can be seen in Figure 7, all three electrodes manifested a decrease of discharge capacity in the initial cycles (up to 50th cycle). Afterward, the specific capacity of the NiS₂:Mo microsphere electrodes increased slightly, without apparent capacity fading, until 120th cycle. However, the specific capacity of the bare NiS₂ electrode was found to decrease gradually. Such a trend might be due to the weak activation process in the NiS₂:Mo microsphere electrodes

in the initial 50 cycles and low Li⁺ ions insertion due to Mo doping, which results in a slight decrease in the specific capacity gain. In addition, partial amorphization of MoO₃ during initial cycling could also lead to an increase in the Li⁺ ion diffusion kinetics, providing more accessible active sites for Li⁺ insertion, and hence causing a gradual increase of the specific capacity. Similar cycling-induced capacity gain has been previously observed for MoO₃-based anode materials.^{30,47} Interestingly, the NiS₂:Mo (5%) microsphere electrode delivered an exceptionally high initial specific capacity of 900 mAh g⁻¹, which exceeded the theoretically predicted specific capacity value of NiS₂ (807 mAh g⁻¹),²¹ as well as previously reported specific capacity values for the TMO/TMS-based anode materials, as shown in Table 1.^{58,61,63–66} Even though

Table 1. Comparison of the Performance of the NiS₂:Mo (5%) Microsphere Electrode with the Performance of Previously Reported TMS and Mo-Based Oxide Nanostructures in LIBs

nanostructured anode materials	current density (mA)	cycle numbers	reversible capacity (mAh g ⁻¹)	reference
ZnS ₂ /CNT nanocomposite	100	200	730	19
NiCo ₂ S ₄ /N-doped carbon	100	100	480	63
NiS ₂ /CoS ₂ NCs encapsulated N-doped carbon	100	100	680	64
NiS ₂ /FeS	10	100	580	65
NiS ₂ /FeS ₂ /N-doped carbon nanorods	100	100	718	59
NiO nanosheets arrays/NiS@Ni ₃ S ₂	100	70	498.5	61
MoO ₃ NPs/Graphite	0.2 C	120	712	66
Ti-doped MoO ₃	200	250	681.2	58
NiS ₂ :Mo microspheres	100	120	713.3	this work

the specific capacity of the electrode decreased gradually up to 50th cycle, it retained a high reversible capacity of 713.3 mAh g⁻¹ even after 120 cycles, with CE as high as 98.43%.

On the other hand, the electrode made of pure NiS₂ microspheres showed a low reversible capacity, and the electrode made of NiS₂:Mo (10%) microspheres suffered an intermediate reversible capacity after 120 cycles. Specifically, the pure NiO₂ and NiS₂:Mo (10%) microsphere electrodes yielded reversible discharge capacities of 286.7 mAh g⁻¹ (95.84% CE) and 603.5 mAh g⁻¹ (97.23% CE) after 120 cycles, respectively. Nevertheless, these values are relatively lower in comparison with the discharge capacity of the NiS₂:Mo (5%) microsphere electrode (713.3 mAh g⁻¹), confirming its superior cycling stability performance. The decrease in rate performance and cycling stability of the NiS₂:Mo (10%) microsphere electrode could be attributed to the excess Mo doping, which leads to the reduction of reversibility of the conversion reaction, as observed in the CV curves presented in Figure 5b. Furthermore, a higher concentration of Mo in the NiS₂ lattice and only partial Mo⁶⁺ ions occupy the Ni²⁺ lattice; consequently, a high concentration of Mo⁶⁺ ions segregates onto the surface of NiS₂ as observed in SEM results in Figure 2e,f. Such high Mo⁶⁺ segregation toward the NiS₂ surface may significantly affect the electrode/electrolyte interface and Li⁺ ion insertion/exertion

process, lowering the overall cycling stability performance of the NiS₂:Mo (10%) electrode.

To understand the electrochemical kinetics of Li ions in the NiS₂:Mo (5%) anode further, its CV curve was recorded with different scan rates in a Li half-cell. Figure 8a presents the CV profiles of the NiS₂:Mo (5%) electrode at different scan rates of 0.1, 0.2, 0.3, 0.4, 0.8, and 1.0 mV s⁻¹. The CV curves acquired at different scan rates have similar shapes. However, the peak current increased with the increase of the scan rate from 0.1 to 1 mVs⁻¹. In general, the total amount of charges stored in the anode material could be contributed by two different effects: (i) The pseudocapacitive effect originated from the electric double layer formation at the electrode–electrolyte interfaces and (ii) the diffusion-controlled insertion process in the faradaic reactions of the redox species. The contribution of these two effects can be evaluated by analyzing the CV response of an electrode at different scan rates, following the power-law relationship⁶⁷

$$i = av^b \quad (3)$$

where a and b are two adjustable parameters, i is the current, and v is the sweep rate. The b value can be obtained from the slopes of $\log(v)$ vs $\log(i)$ plots, as displayed in Figure 8b. The value of b suggests whether the reaction is limited by the diffusion-controlled process (when $b = 0.5$) or capacitive effect (when $b = 1.0$). From the $\log(i)$ vs $\log(v)$ plots in Figure 8b, the estimated b values for the anodic and cathodic peaks were about 0.95, 0.78, 0.84, 0.92, and 0.86 for peaks 1, 2, 3, 4, and 5, respectively. The b values estimated for the anodic and cathodic peaks suggest that the charge storage in the NiS₂:Mo (5%) electrode is mainly contributed by the pseudocapacitive process. In fact, similar current response behaviors have been seen for many metal sulfide-based anode materials.^{19,20,68}

To estimate the capacitive contribution in the total stored charges for NiS₂:Mo (5%) quantitatively, the obtained current can be described by the following equation⁶⁹

$$i(V) = k_1v + k_2v^{1/2} \quad (4)$$

where k_1 and k_2 are constants at a certain potential, k_1v and $k_2v^{1/2}$ are associated with the surface-induced capacitive effect and diffusion-controlled insertion process, respectively. The pseudocapacitive contributions can be separated from the whole area of the CV curve by estimating the ratio of the integral area of pseudocapacitive currents (red color) as shown in Figure 8c. As can be seen in Figure 8c, the estimated pseudocapacitive contribution for NiS₂:Mo (5%) at a scan rate of 0.1 mV s⁻¹ covers the major portion of the CV curve (red-colored shaded area). Figure 8d shows the bar chart diagram, summarizing the ratio between diffusion-controlled contribution and pseudocapacitive process at varied scan rates. The estimated pseudocapacitive contributions were about 60.2, 66.1, 69.8, 73.1, 81.0, and 84.7% at the scan rates of 0.1, 0.2, 0.3, 0.4, 0.8, and 1.0 mV s⁻¹, respectively. As can be noticed, the percentage of pseudocapacitive contribution increases from 60.2 to 84.7% with an increase in scan rate from 0.1 to 1.0 mV s⁻¹. The results confirm that the high charge storage and enhanced rate performance of the NiS₂:Mo (5%) microsphere electrode are attributed to its pseudocapacitive charge storage behavior, which leads to a fast Li⁺ ion insertion/extraction and enhancement of cycling life of the electrode.

To identify if there occurred any structural change in the NiS₂:Mo (5%) electrode upon performing cycling stability tests, the morphology of the electrode was examined by the

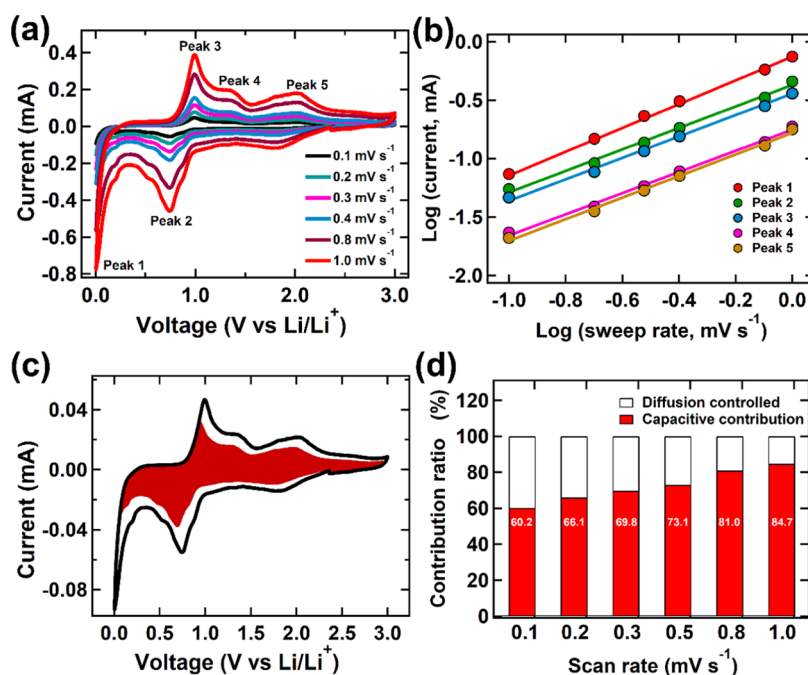


Figure 8. (a) CV curves of NiS₂:Mo (5%) microsphere electrodes at various scan rates from 0.1 to 1.0 mVs⁻¹; (b) log (I) vs log (V) plots for the electrode at each redox peak; (c) CV curves showing the separation of pseudocapacitive currents (red region) from the total current at a scan rate of 1 mVs⁻¹; (d) bar chart diagram showing the pseudocapacitive contribution at different scan rates ranging from 0.1 to 1 mVs⁻¹.

SEM and TEM (Figures S3 and S4, Supporting Information). The SEM images of the utilized (in 120 charge–discharge cycles) electrode revealed a very similar morphology as that of the unused electrode, indicating no significant damage occurred in the electrode or the material due to charge–discharge cycling (Figure S3). Furthermore, the TEM images obtained after the cycling tests (120 charge–discharge cycles) confirm that the NiS₂:Mo (5%) microspheres maintain their original morphology, and no cracks or aggregation occurred (Figure S4, Supporting Information). All of these results provide enough evidence of the structural stability of NiS₂:Mo microspheres, which is an essential requirement to overcome the challenges associated with the volume expansion of the anode material during charge–discharge cycling, and assure the long cycling stability of the fabricated anode.

Charge transfer resistance at the electrode/electrolyte solution interface was probed by recording the electrochemical impedance spectroscopy (EIS) spectra of the anodes. Figure 9 presents the Nyquist plots for the NiS₂, NiS₂:Mo (5%), and NiS₂:Mo (10%) microsphere electrodes. The inset (lower) of Figure 9 depicts the Randles equivalent circuit model utilized to fit the EIS spectra, which consists of charge transfer resistance (R_{ct}), solution resistance (R_s), constant phase element (CPE), and Warburg impedance (Z_w). As it is evident from the inset (upper) of Figure 9, the Nyquist plots for all three samples exhibited a high-frequency semicircle, followed by a quasi-linear variation in the low-frequency side. The R_{ct} at the electrode/electrolyte interface can be obtained directly from the semicircle, while the quasi-linear part represents the solid-state diffusion resistance of Li⁺ in the electrodes.^{31,70} It is evident from Figure 9 that the NiS₂:Mo (5%) microsphere sample presents a semicircle of the smallest diameter, indicating its smallest R_{ct} among the three electrodes. The R_{ct} values estimated for the NiS₂, NiS₂:Mo (5%), and NiS₂:Mo (10%) microsphere electrodes were 17.28, 15.61, and 16.79 Ω , respectively. The EIS results indicated that the NiS₂:Mo (5%)

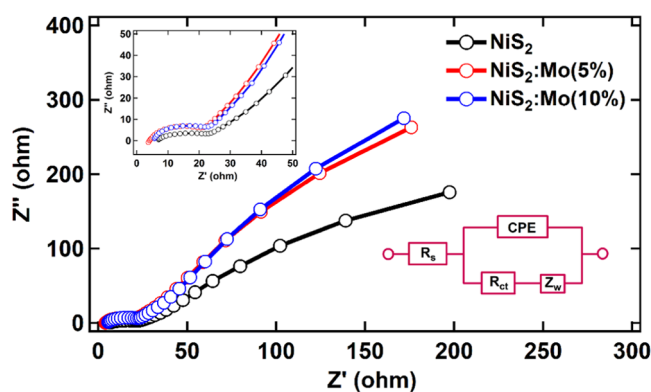


Figure 9. Nyquist plots for the pure NiS₂, NiS₂:Mo (5%), and NiS₂:Mo (10%) microsphere electrodes. Insets show the proposed equivalent circuit (lower) and magnified view of the high-frequency region (upper).

microsphere electrode had higher electrical conductivity than the pristine NiS₂ and NiS₂:Mo (10%) microsphere electrodes.

Based on the above experimental results, the improved electrochemical lithium storage performance of the NiS₂:Mo (5%) microsphere anode could be ascribed to several factors. First, incorporating Mo in low concentration (i.e., 5 wt %) significantly improves the electronic conductivity (Figure 9) and structural stability of NiS₂, which facilitate the ion and mass transfer between the electrolyte and the electrode interface. As a result, the anode made of NiS₂:Mo (5%) exhibits a long cycling life. Second, the unique microsphere morphology of the as-prepared NiS₂:Mo microspheres could provide an enhanced specific surface area and promote fast Li⁺ ion insertion/exertion kinetics. Thus, the results obtained in this study clearly demonstrate that the anodes fabricated with NiS₂:Mo (5%) microspheres exhibit superior electrochemical performance toward lithium storage. The green synthesis

protocol implemented in the preparation of NiS₂:Mo microspheres can be easily implemented to fabricate other metal sulfide and metal oxide microstructures with enhanced electrochemical properties.

4. CONCLUSIONS

In summary, an environmentally friendly, hydrothermal synthesis strategy was designed to prepare porous NiS₂:Mo microspheres with varied Mo contents to utilize them as anode materials in LIBs. We demonstrate that Mo doping improves the electronic conductivity, charge transfer efficiency, and structural stability of the NiS₂ microspheres. The utilization of NiS₂:Mo microspheres in LIB anodes renders exceptional lithium storage capacity, high reversible specific capacity, along with prolonged cycling stability and good rate capability performance. In particular, Mo doping in moderate concentration (i.e., 5 wt %) enhances the initial specific capacity of the NiS₂ microsphere electrodes to as high as 1605 mAh g⁻¹ at 0.1 A g⁻¹ current density, along with a drastic enhancement of rate capability and reversible specific discharge capacity (713.3 mAh g⁻¹) even after 120 cycles. Moreover, even after 120 cycles of charge–discharge cycling, the Coulombic efficiency of the electrode remains around 98.42%. The obtained results clearly demonstrate the advantages of the utilized synthesis strategy for fabricating porous metal sulfide microstructures for utilization as high-capacity anode materials for next-generation LIBs.

■ ASSOCIATED CONTENT

SI Supporting Information

The Supporting Information is available free of charge at <https://pubs.acs.org/doi/10.1021/acsaem.2c00340>.

EDX analysis of the NiS₂:Mo microspheres; EDX mapping analysis; and SEM and TEM images of NiS₂:Mo microsphere electrodes after 120 cycles (PDF)

■ AUTHOR INFORMATION

Corresponding Author

Siva Kumar Krishnan – CONACYT-Instituto de Física, Benemérita Universidad Autónoma de Puebla, Puebla 72570, Mexico; orcid.org/0000-0002-9672-9335; Email: sivakumar@ifuap.buap.mx

Authors

Paskalis Sahaya Murphin Kumar – Department of Civil and Environmental Engineering, Yonsei University, Seoul 03722, Republic of Korea; Department of Medicinal and Applied Chemistry & Research Centre for Environmental Medicine, Kaohsiung Medical University, Kaohsiung City 80756, Taiwan; orcid.org/0000-0002-2688-1825

Vinothkumar Ponnusamy – Department of Medicinal and Applied Chemistry & Research Centre for Environmental Medicine, Kaohsiung Medical University, Kaohsiung City 80756, Taiwan; Department of Medical Research, Kaohsiung Medical University Hospital, Kaohsiung City 80756, Taiwan; orcid.org/0000-0003-2112-2085

Hyoung-il Kim – Department of Civil and Environmental Engineering, Yonsei University, Seoul 03722, Republic of Korea; orcid.org/0000-0003-4358-1442

Martín Adelaido Hernández-Landaverde – CINVESTAV-Unidad Querétaro, 76230 Querétaro, México

Umapada Pal – Instituto de Física, Benemérita Universidad Autónoma de Puebla, Puebla 72570, Mexico; orcid.org/0000-0002-5665-106X

Complete contact information is available at: <https://pubs.acs.org/10.1021/acsaem.2c00340>

Notes

The authors declare no competing financial interest.

■ ACKNOWLEDGMENTS

This work was supported (in part) by the Yonsei University Research Fund (Yonsei Frontier Lab. Young Researcher Supporting Program) of 2022. SKK thanks CONACyT, Mexico, for the help extended through the cathedra of CONACyT project. Financial supports extended by VIEP-BUAP and CONACyT, Mexico (Grant #CB A1-S-26720), are thankfully acknowledged.

■ REFERENCES

- (1) Wu, F.; Maier, J.; Yu, Y. Guidelines and Trends for Next-Generation Rechargeable Lithium and Lithium-Ion Batteries. *Chem. Soc. Rev.* **2020**, *49*, 1569–1614.
- (2) Liu, D. H.; Bai, Z.; Li, M.; Yu, A.; Luo, D.; Liu, W.; Yang, L.; Lu, J.; Amine, K.; Chen, Z. Developing High Safety Li-Metal Anodes for Future High-Energy Li-Metal Batteries: Strategies and Perspectives. *Chem. Soc. Rev.* **2020**, *49*, 5407–5445.
- (3) Ozawa, K. Lithium-Ion Rechargeable Batteries with LiCoO₂ and Carbon Electrodes: The LiCoO₂/C System. *Solid State Ionics* **1994**, *69*, 212–221.
- (4) Cano, Z. P.; Banham, D.; Ye, S.; Hintennach, A.; Lu, J.; Fowler, M.; Chen, Z. Batteries and Fuel Cells for Emerging Electric Vehicle Markets. *Nat. Energy* **2018**, *3*, 279–289.
- (5) Dunn, B.; Kamath, H.; Tarascon, J. M. Electrical Energy Storage for the Grid: A Battery of Choices. *Science* **2011**, *334*, 928–935.
- (6) Lu, J.; Chen, Z.; Ma, Z.; Pan, F.; Curtiss, L. A.; Amine, K. The Role of Nanotechnology in the Development of Battery Materials for Electric Vehicles. *Nat. Nanotechnol.* **2016**, *11*, 1031–1038.
- (7) Zeng, X.; Li, M.; Abd El-Hady, D.; Alshitari, W.; Al-Bogami, A. S.; Lu, J.; Amine, K. Commercialization of Lithium Battery Technologies for Electric Vehicles. *Adv. Energy Mater.* **2019**, *9*, No. 1900161.
- (8) Cai, X.; Lai, L.; Shen, Z.; Lin, J. Graphene and Graphene-Based Composites as Li-Ion Battery Electrode Materials and Their Application in Full Cells. *J. Mater. Chem. A* **2017**, *5*, 15423–15446.
- (9) Zheng, S.; Zhang, H. Y.; Fan, J. C.; Xu, Q. J.; Min, Y. L. In Situ Construction of Aramid Nanofiber Membrane on Li Anode as Artificial SEI Layer Achieving Ultra-High Stability. *Small* **2021**, *17*, No. 2102347.
- (10) Shi, Z.; Guo, W. Y.; Zhou, L.; Xu, Q.; Min, Y. A 3D Fiber Skeleton Reinforced PEO-Based Polymer Electrolyte for High Rate and Ultra-Long Cycle All-Solid-State Batteries. *J. Mater. Chem. A* **2021**, *9*, 21057–21070.
- (11) Zhang, X. L.; Guo, W. Y.; Zhou, L.; Xu, Q.; Min, Y. Surface-Modified Boron Nitride as a Filler to Achieve High Thermal Stability of Polymer Solid-State Lithium-Metal Batteries. *J. Mater. Chem. A* **2021**, *9*, 20530–20543.
- (12) Reddy, M. V.; Subba Rao, G. V.; Chowdari, B. V. R. Metal Oxides and Oxyalts as Anode Materials for Li Ion Batteries. *Chem. Rev.* **2013**, *113*, 5364–5457.
- (13) Li, Q.; Li, H.; Xia, Q.; Hu, Z.; Zhu, Y.; Yan, S.; Ge, C.; Zhang, Q.; Wang, X.; Shang, X.; Fan, S.; Long, Y.; Gu, L.; Miao, G. X.; Yu, G.; Moodera, J. S. Extra Storage Capacity in Transition Metal Oxide Lithium-Ion Batteries Revealed by in Situ Magnetometry. *Nat. Mater.* **2021**, *20*, 76–83.
- (14) Lee, J. M.; Singh, G.; Cha, W.; Kim, S.; Yi, J.; Hwang, S. J.; Vinu, A. Recent Advances in Developing Hybrid Materials for Sodium-Ion Battery Anodes. *ACS Energy Lett.* **2020**, *5*, 1939–1966.

- (15) Grey, C. P.; Hall, D. S. Prospects for Lithium-Ion Batteries and beyond—a 2030 Vision. *Nat. Commun.* **2020**, *11*, No. 6279.
- (16) Xu, X.; Liu, W.; Kim, Y.; Cho, J. Nanostructured Transition Metal Sulfides for Lithium Ion Batteries: Progress and Challenges. *Nano Today* **2014**, *9*, 604–630.
- (17) Fang, Y.; Luan, D.; Lou, X. W. Recent Advances on Mixed Metal Sulfides for Advanced Sodium-Ion Batteries. *Adv. Mater.* **2020**, *32*, No. 2002976.
- (18) Xiao, Y.; Lee, S. H.; Sun, Y. K. The Application of Metal Sulfides in Sodium Ion Batteries. *Adv. Energy Mater.* **2017**, *7*, 1601329–1601249.
- (19) Hou, T.; Liu, B.; Sun, X.; Fan, A.; Xu, Z.; Cai, S.; Zheng, C.; Yu, G.; Tricoli, A. Covalent Coupling-Stabilized Transition-Metal Sulfide/Carbon Nanotube Composites for Lithium/Sodium-Ion Batteries. *ACS Nano* **2021**, *15*, 6735–6746.
- (20) Peng, Q.; Zhang, S.; Yang, H.; Sheng, B.; Xu, R.; Wang, Q.; Yu, Y. Boosting Potassium Storage Performance of the Cu₂S Anode via Morphology Engineering and Electrolyte Chemistry. *ACS Nano* **2020**, *14*, 6024–6033.
- (21) Wang, T.; Hu, P.; Zhang, C.; Du, H.; Zhang, Z.; Wang, X.; Chen, S.; Xiong, J.; Cui, G. Nickel Disulfide-Graphene Nanosheets Composites with Improved Electrochemical Performance for Sodium Ion Battery. *ACS Appl. Mater. Interfaces* **2016**, *8*, 7811–7817.
- (22) Zhao, J.; Zhao, D.; Li, L.; Zhou, L.; Liang, X.; Wu, Z.; Jiang, Z. J. Defect-Rich, Mesoporous Cobalt Sulfide Hexagonal Nanosheets as Superior Sulfur Hosts for High-Rate, Long-Cycle Rechargeable Lithium-Sulfur Batteries. *J. Phys. Chem. C* **2020**, *124*, 12259–12268.
- (23) Han, P.; Chung, S. H.; Manthiram, A. Thin-Layered Molybdenum Disulfide Nanoparticles as an Effective Polysulfide Mediator in Lithium-Sulfur Batteries. *ACS Appl. Mater. Interfaces* **2018**, *10*, 23122–23130.
- (24) Zhang, K.; Park, M.; Zhou, L.; Lee, G. H.; Shin, J.; Hu, Z.; Chou, S. L.; Chen, J.; Kang, Y. M. Cobalt-Doped FeS₂ Nanospheres with Complete Solid Solubility as a High-Performance Anode Material for Sodium-Ion Batteries. *Angew. Chem., Int. Ed.* **2016**, *55*, 12822–12826.
- (25) Douglas, A.; Carter, R.; Oakes, L.; Share, K.; Cohn, A. P.; Pint, C. L. Ultrafine Iron Pyrite (FeS₂) Nanocrystals Improve Sodium-Sulfur and Lithium-Sulfur Conversion Reactions for Efficient Batteries. *ACS Nano* **2015**, *9*, 11156–11165.
- (26) Guo, H.; Tang, L.; Tian, Q.; Chu, Y.; Shi, B.; Yin, X.; Huo, H.; Han, X.; Yang, C.; Wang, C.; Tang, K.; Wang, C.; Zhang, X.; Wang, J.; Kong, L.; Lu, Z. Cobalt-Doped NiS₂ Micro/Nanostructures with Complete Solid Solubility as High-Performance Cathode Materials for Actual High-Specific-Energy Thermal Batteries. *ACS Appl. Mater. Interfaces* **2020**, *12*, 50377–50387.
- (27) Zhang, J.; Li, S.; Hu, R.; Yuan, B. An Effective Ni(OH)₂ Optimization Strategy via Cu²⁺ and Ni³⁺ Co-Doping for High Capacity and Long Life-Span Lithium Ion Batteries. *Ionics* **2021**, *27*, 2053–2066.
- (28) Hu, Q.; Li, W.; Abouelamaiem, D. I.; Xu, C.; Jiang, H.; Han, W.; He, G. Hollow Cu-Doped NiO Microspheres as Anode Materials with Enhanced Lithium Storage Performance. *RSC Adv.* **2019**, *9*, 20963–20967.
- (29) Zhao, Q.; Guo, Z.; Wang, L.; Wu, Y.; Butt, F. K.; Zhu, Y.; Xu, X.; Ma, X.; Cao, C. Mo-Modified P2-Type Manganese Oxide Nanoplates with an Oriented Stacking Structure and Exposed {010} Active Facets as a Long-Life Sodium-Ion Battery Cathode. *ACS Appl. Mater. Interfaces* **2019**, *11*, 30819–30827.
- (30) Chen, F.; Wang, J.; Huang, L.; Bao, H.; Shi, Y. Ordered Mesoporous Crystalline Mo-Doped WO₂ Materials with High Tap Density as Anode Material for Lithium Ion Batteries. *Chem. Mater.* **2016**, *28*, 608–617.
- (31) Murphin Kumar, P. S.; Al-Muhtaseb, A. H.; Kumar, G.; Vinu, A.; Cha, W.; Villanueva Cab, J.; Pal, U.; Krishnan, S. K. Piper Longum Extract-Mediated Green Synthesis of Porous Cu₂O:Mo Microspheres and Their Superior Performance as Active Anode Material in Lithium-Ion Batteries. *ACS Sustainable Chem. Eng.* **2020**, *8*, 14557–14567.
- (32) Shannon, R. D.; Prewitt, C. T. Effective ionic radii and crystal chemistry. *J. Inorg. Nucl. Chem.* **1970**, *32*, 1427–1441.
- (33) Breuer, O.; Chakraborty, A.; Liu, J.; Kravchuk, T.; Burstein, L.; Grinblat, J.; Kauffman, Y.; Gladkih, A.; Nayak, P.; Tsubery, M.; Frenkel, A. I.; Talianker, M.; Major, D. T.; Markovsky, B.; Aurbach, D. Understanding the Role of Minor Molybdenum Doping in LiNi_{0.5}Co_{0.2}Mn_{0.3}O₂ Electrodes: From Structural and Surface Analyses and Theoretical Modeling to Practical Electrochemical Cells. *ACS Appl. Mater. Interfaces* **2018**, *10*, 29608–29621.
- (34) Wang, X.; Guo, K.; Xia, Y.; Min, Y.; Xu, Q. Nonstoichiometric Molybdenum Trioxide Adjustable Energy Barrier Enabling Ultralong-Life All-Solid-State Lithium Batteries. *ACS Appl. Mater. Interfaces* **2021**, *13*, 60907–60920.
- (35) Wang, J.; Tang, H.; Zhang, L.; Ren, H.; Yu, R.; Jin, Q.; Qi, J.; Mao, D.; Yang, M.; Wang, Y.; Liu, P.; Zhang, Y.; Wen, Y.; Gu, L.; Ma, G.; Su, Z.; Tang, Z.; Zhao, H.; Wang, D. Multi-Shelled Metal Oxides Prepared via an Anion-Adsorption Mechanism for Lithium-Ion Batteries. *Nat. Energy* **2016**, *1*, No. 16184.
- (36) Wang, W.; Li, J.; Jin, Q.; Liu, Y.; Zhang, Y.; Zhao, Y.; Wang, X.; Nurpeissova, A.; Bakenov, Z. Rational Construction of Sulfur-Deficient NiCo₂S₄-XHollow Microspheres as an Effective Polysulfide Immobilizer toward High-Performance Lithium/Sulfur Batteries. *ACS Appl. Energy Mater.* **2021**, *4*, 1687–1695.
- (37) Vu, A.; Qian, Y.; Stein, A. Porous Electrode Materials for Lithium-Ion Batteries—How to Prepare Them and What Makes Them Special. *Adv. Energy Mater.* **2012**, *2*, 1056–1085.
- (38) Chen, J. S.; Guan, C.; Gui, Y.; Blackwood, D. J. Rational Design of Self-Supported Ni₃S₂ Nanosheets Array for Advanced Asymmetric Supercapacitor with a Superior Energy Density. *ACS Appl. Mater. Interfaces* **2017**, *9*, 496–504.
- (39) Zang, X.; Dai, Z.; Yang, J.; Zhang, Y.; Huang, W.; Dong, X. Template-Assisted Synthesis of Nickel Sulfide Nanowires: Tuning the Compositions for Supercapacitors with Improved Electrochemical Stability. *ACS Appl. Mater. Interfaces* **2016**, *8*, 24645–24651.
- (40) Mao, Y.; Park, T. J.; Zhang, F.; Zhou, H.; Wong, S. S. Environmentally Friendly Methodologies of Nanostructure Synthesis. *Small* **2007**, *3*, 1122–1139.
- (41) Datta, S.; Jo, C.; De Volder, M.; Torrente-Murciano, L. Morphological Control of Nanostructured V₂O₅ by Deep Eutectic Solvents. *ACS Appl. Mater. Interfaces* **2020**, *12*, 18803–18812.
- (42) Tammina, S. K.; Mandal, B. K.; Ranjan, S.; Dasgupta, N. Cytotoxicity Study of Piper Nigrum Seed Mediated Synthesized SnO₂ Nanoparticles towards Colorectal (HCT116) and Lung Cancer (A549) Cell Lines. *J. Photochem. Photobiol., B* **2017**, *166*, 158–168.
- (43) Nakkala, J. R.; Mata, R.; Sadras, S. R. The Antioxidant and Catalytic Activities of Green Synthesized Gold Nanoparticles from Piper Longum Fruit Extract. *Process Saf. Environ. Prot.* **2016**, *100*, 288–294.
- (44) Reddy, N. J.; Nagoor Vali, D.; Rani, M.; Rani, S. S. Evaluation of Antioxidant, Antibacterial and Cytotoxic Effects of Green Synthesized Silver Nanoparticles by Piper Longum Fruit. *Mater. Sci. Eng. C* **2014**, *34*, 115–122.
- (45) Liu, H.; Ni, Y.; Han, M.; Liu, Q.; Xu, Z.; Hong, J.; Ma, X. A Facile Template-Free Route for Synthesis of Hollow Hexagonal ZnS Nano- and Submicro-Spheres. *Nanotechnology* **2005**, *16*, 2908–2912.
- (46) Wang, W.; Qin, J.; Yin, Z.; Cao, M. Achieving Fully Reversible Conversion in MoO₃ for Lithium Ion Batteries by Rational Introduction of CoMoO₄. *ACS Nano* **2016**, *10*, 10106–10116.
- (47) Ab Malik Marwan, N. A.; Md Jahangir Alam, N. N.; Samat, M. H.; Mohyedin, M. Z.; Hussin, N. H.; Hassan, O. H.; Yahya, M. Z. A.; Mohamad Taib, M. F. Bin. First-Principles Studies on Structural, Electronic and Optical Properties of Fe-Doped NiS₂ Counter Electrode for Dye-Sensitized Solar Cells Using Dft+U. *Sci. Res. J.* **2020**, *17*, 81–98.
- (48) Zhou, L.; Yang, L.; Yuan, P.; Zou, J.; Wu, Y.; Yu, C. α -MoO₃ Nanobelts: A High Performance Cathode Material for Lithium Ion Batteries. *J. Phys. Chem. C* **2010**, *114*, 21868–21872.
- (49) Luo, P.; Zhang, H.; Liu, L.; Zhang, Y.; Deng, J.; Xu, C.; Hu, N.; Wang, Y. Targeted Synthesis of Unique Nickel Sulfide (NiS, Ni₃S₂)

Microarchitectures and the Applications for the Enhanced Water Splitting System. *ACS Appl. Mater. Interfaces* **2017**, *9*, 2500–2508.

(50) Zhang, Q.; Peng, G.; Mwizerwa, J. P.; Wan, H.; Cai, L.; Xu, X.; Yao, X. Nickel Sulfide Anchored Carbon Nanotubes for All-Solid-State Lithium Batteries with Enhanced Rate Capability and Cycling Stability. *J. Mater. Chem. A* **2018**, *6*, 12098–12105.

(51) Liu, H.; Ma, X.; Rao, Y.; Liu, Y.; Liu, J.; Wang, L.; Wu, M. Heteromorphic NiCo₂S₄/Ni₃S₂/Ni Foam as a Self-Standing Electrode for Hydrogen Evolution Reaction in Alkaline Solution. *ACS Appl. Mater. Interfaces* **2018**, *10*, 10890–10897.

(52) Lu, M.; Gao, N.; Zhang, X. J.; Wang, G. S. Reduced Graphene Oxide Decorated with Octahedral NiS₂/NiS Nanocrystals: Facile Synthesis and Tunable High Frequency Attenuation. *RSC Adv.* **2019**, *9*, 5550–5556.

(53) Balaghi, S. E.; Triana, C. A.; Patzke, G. R. Molybdenum-Doped Manganese Oxide as a Highly Efficient and Economical Water Oxidation Catalyst. *ACS Catal.* **2020**, *10*, 2074–2087.

(54) Orozco, C.; Melendez, A.; Manadhar, S.; Singamaneni, S. R.; Reddy, K. M.; Gandha, K.; Niebedim, I. C.; Ramana, C. V. Effect of Molybdenum Incorporation on the Structure and Magnetic Properties of Cobalt Ferrite. *J. Phys. Chem. C* **2017**, *121*, 25463–25471.

(55) Zhang, Y.; Lv, C.; Wang, X.; Chen, S.; Li, D.; Peng, Z.; Yang, D. Boosting Sodium-Ion Storage by Encapsulating NiS (CoS) Hollow Nanoparticles into Carbonaceous Fibers. *ACS Appl. Mater. Interfaces* **2018**, *10*, 40531–40539.

(56) Liu, T.; Lin, L.; Bi, X.; Tian, L.; Yang, K.; Liu, J.; Li, M.; Chen, Z.; Lu, J.; Amine, K.; Xu, K.; Pan, F. In Situ Quantification of Interphasial Chemistry in Li-Ion Battery. *Nat. Nanotechnol.* **2019**, *14*, 50–56.

(57) Yu, D. J.; Yuan, Y. F.; Zhang, D.; Yin, S. M.; Lin, J. X.; Rong, Z.; Yang, J. L.; Chen, Y. B.; Guo, S. Y. Nickel Cobalt Sulfide Nanotube Array on Nickel Foam as Anode Material for Advanced Lithium-Ion Batteries. *Electrochim. Acta* **2016**, *198*, 280–286.

(58) Yan, Y.; Li, S.; Yuan, B.; Hu, R.; Yang, L.; Liu, J.; Wang, Y.; Luo, Z.; Ying, H.; Zhang, S.; Han, W. Q.; Zhu, M. Flowerlike Ti-Doped MoO₃ Conductive Anode Fabricated by a Novel NiTi Dealloying Method: Greatly Enhanced Reversibility of the Conversion and Intercalation Reaction. *ACS Appl. Mater. Interfaces* **2020**, *12*, 8240–8248.

(59) Wang, S.; Ning, P.; Huang, S.; Wang, W.; Fei, S.; He, Q.; Zai, J.; Jiang, Y.; Hu, Z.; Qian, X.; Chen, Z. Multi-Functional NiS₂/FeS₂/N-Doped Carbon Nanorods Derived from Metal-Organic Frameworks with Fast Reaction Kinetics for High Performance Overall Water Splitting and Lithium-Ion Batteries. *J. Power Sources* **2019**, *436*, No. 226857.

(60) Xie, H.; Chen, M.; Wu, L. Hierarchical Nanostructured NiS/MoS₂/C Composite Hollow Spheres for High Performance Sodium-Ion Storage Performance. *ACS Appl. Mater. Interfaces* **2019**, *11*, 41222–41228.

(61) Wu, X.; Li, S.; Xu, Y.; Wang, B.; Liu, J.; Yu, M. Hierarchical Heterostructures of NiO Nanosheet Arrays Grown on Pine Twig-like B-NiS@Ni₃S₂ Frameworks as Free-Standing Integrated Anode for High-Performance Lithium-Ion Batteries. *Chem. Eng. J.* **2019**, *356*, 245–254.

(62) Zhang, Z.; Zhao, H.; Xia, Q.; Allen, J.; Zeng, Z.; Gao, C.; Li, Z.; Du, X.; Świerczek, K. High Performance Ni₃S₂/Ni Film with Three Dimensional Porous Architecture as Binder-Free Anode for Lithium Ion Batteries. *Electrochim. Acta* **2016**, *211*, 761–767.

(63) Yuan, D.; Huang, G.; Yin, D.; Wang, X.; Wang, C.; Wang, L. Metal-Organic Framework Template Synthesis of NiCo₂S₄@C Encapsulated in Hollow Nitrogen-Doped Carbon Cubes with Enhanced Electrochemical Performance for Lithium Storage. *ACS Appl. Mater. Interfaces* **2017**, *9*, 18178–18186.

(64) Lin, Y.; Qiu, Z.; Li, D.; Ullah, S.; Hai, Y.; Xin, H.; Liao, W.; Yang, B.; Fan, H.; Xu, J.; Zhu, C. NiS₂@CoS₂ Nanocrystals Encapsulated in N-Doped Carbon Nanocubes for High Performance Lithium/Sodium Ion Batteries. *Energy Storage Mater.* **2018**, *11*, 67–74.

(65) Liang, K.; Marcus, K.; Zhang, S.; Zhou, L.; Li, Y.; De Oliveira, S. T.; Orlovskaya, N.; Sohn, Y. H.; Yang, Y. NiS₂/FeS Holey Film as Freestanding Electrode for High-Performance Lithium Battery. *Adv. Energy Mater.* **2017**, *7*, No. 1701309.

(66) Tao, T.; Glushenkov, A. M.; Zhang, C.; Zhang, H.; Zhou, D.; Guo, Z.; Liu, H. K.; Chen, Q.; Hu, H.; Chen, Y. MoO₃ Nanoparticles Dispersed Uniformly in Carbon Matrix: A High Capacity Composite Anode for Li-Ion Batteries. *J. Mater. Chem.* **2011**, *21*, 9350–9355.

(67) Wang, X.; Shen, G. Intercalation Pseudo-Capacitive TiNb₂O₇@carbon Electrode for High-Performance Lithium Ion Hybrid Electrochemical Supercapacitors with Ultrahigh Energy Density. *Nano Energy* **2015**, *15*, 104–115.

(68) Chen, Y.; Hu, X.; Evanko, B.; Sun, X.; Li, X.; Hou, T.; Cai, S.; Zheng, C.; Hu, W.; Stucky, G. D. High-Rate FeS₂/CNT Neural Network Nanostructure Composite Anodes for Stable, High-Capacity Sodium-Ion Batteries. *Nano Energy* **2018**, *46*, 117–127.

(69) Lan, Y.; Zhao, H.; Zong, Y.; Li, X.; Sun, Y.; Feng, J.; Wang, Y.; Zheng, X.; Du, Y. Phosphorization Boosts the Capacitance of Mixed Metal Nanosheet Arrays for High Performance Supercapacitor Electrodes. *Nanoscale* **2018**, *10*, 11775–11781.

(70) Zhang, S. S.; Xu, K.; Jow, T. R. Electrochemical Impedance Study on the Low Temperature of Li-Ion Batteries. *Electrochim. Acta* **2004**, *49*, 1057–1061.

Recommended by ACS

Heterostructured NiS/TiO₂ Nanosheets Assembled into Microflowers with Enhanced Cycling Stability for Sodium-Ion Storage

Guangdi Zhang, Yongyao Xia, *et al.*

APRIL 21, 2023

ACS APPLIED ENERGY MATERIALS

READ 

Self-Assembled Hierarchical Silkmoth-Type Bimetallic Sulfide (NiMo₃S₄) Nanostructures Developed on S-g-C₃N₄ Sheets: Promising Electrode Material for Supercapacitors

Mohan Reddy Pallavolu, Sang Woo Joo, *et al.*

JANUARY 02, 2023

ACS APPLIED ENERGY MATERIALS

READ 

Improving the Electrochemical Performance of Li-S Batteries via a MnCo₂S₄-CoS_{1.097} Heterostructure with a Hollow Structure and High Catalytic Activity

Xi Zhou, Xianyou Wang, *et al.*

SEPTEMBER 29, 2022

ACS APPLIED ENERGY MATERIALS

READ 

Double-Layer Carbon Encapsulated Co Particles Combined with Ionic Liquid for Enhancing Electrochemical Detection of Oxygen

Wenyan Yin, Jun Wang, *et al.*

FEBRUARY 06, 2023

ACS SUSTAINABLE CHEMISTRY & ENGINEERING

READ 

Get More Suggestions >